An analysis of the surface generation mechanics of the elliptical vibration texturing process

Ping Guo [a,*], Kornel F. Ehmann [b]

[a] Department of Mechanical Engineering, Northwestern University, 2145 Sheridan Road, Room B110, Evanston, IL-60208, USA
[b] Department of Mechanical Engineering, Northwestern University, 2145 Sheridan Road, Room A215, Evanston, IL-60208, USA

ABSTRACT

The elliptical vibration texturing process is a vibration assisted machining method for the fast generation of micro structured surfaces. It adds a higher order motion component to the cutting tool that leads to periodic changes in the cutting depth during the machining process. This results in the creation of micro-dimples on the machined surface, whose shape is a function of the tool geometry and trajectory. This paper studies the surface generation mechanics of the elliptical vibration texturing process through experimentation and modeling. A surface generation algorithm is presented for this newly developed process. The model fully describes the motion and the 3D geometry of the cutting tool including its rake face, flank face, and the cutting edge, since all these tool features influence the topography of the generated surface. Since the process takes place in the micro/meso-scale cutting regime, the model includes the minimum chip thickness and elastic recovery effects. The experimental results are shown to validate the simulation model. The simulation model is used to characterize the influences of the process parameters on the texture patterns. The effects of the tool geometry on the process, including the cutting edge radius, are also analyzed.

© 2012 Elsevier Ltd. All rights reserved.

1. Introduction

The elliptical vibration texturing process adds a tertiary motion component to the cutting tool tip, which is a higher order motion besides the conventional cutting and feed motions (primary and secondary motions). It introduces deliberate and controllable vibrations between the cutting tool and the workpiece. The cutting tool vibrates along an elliptical trajectory, which imposes textures (dimples) onto the workpiece surface as shown in Fig. 1. The shape and pattern of the textures depend on the shape of the vibration trajectory (frequency and amplitude), the cutting speed and feed rate, as well as on tool geometry.

The process establishes a fast and accurate manufacturing method for micro-structured surface generation, which has many potential applications in friction reduction [1], self-cleaning surfaces [2], diffraction gratings [3], etc. It sets itself apart from other existing processes, such as laser ablation, micro machining, and micro forming, by its flexibility, efficiency and accuracy. The new process is adapted from the micro machining process. It not only holds the benefits of flexibility and accuracy from micro machining, but also dramatically increases the production rate.

This process is inspired by the idea of the elliptical vibration assisted cutting (EVC) process. Early EVC processes utilized one-dimensional vibrations in the cutting direction, which turns the continuous cutting process into an intermittent process. The EVC process reduces the contact time between the tool and the workpiece, which makes it possible to machine steel by diamond tools and to achieve optical quality surfaces [4]. Later, Moriwaki and Shamoto [5] introduced tool vibrations in both the cutting and chip flow directions in the orthogonal cutting model. This arrangement significantly reduces the chip thickness and brings various benefits such as reduced cutting forces, better surface finish, burr suppression, and longer tool life [6,7]. The EVC process also offers advantages in the ductile cutting of brittle materials. By reducing the instantaneous chip thickness [8] and creating a large negative effective rake angle, the EVC process remarkably increases the nominal critical depth of cut in conventional cutting, below which the brittle material deforms plastically and forms a crack-free surface [9].

The schematic of the cylindrical turning operation is shown in Fig. 2, which depicts the differences between the EVC and the elliptical vibration texturing processes. Unlike the EVC process, the elliptical vibration texturing process adds vibrations in the cutting and radial directions, while in the EVC process the vibrations are in the cutting and feed directions. The radial vibration dictates the texturing process by varying the cutting depth perpendicular to the workpiece surface. The vibration in

* Corresponding author. Tel.: 1 847 467 1851; fax: 1 847 491 3915.
  E-mail addresses: Pingguo2009@u.northwestern.edu (P. Guo),
k-ehmann@northwestern.edu (K.F. Ehmann).

Nomenclature

A_x, A_y, A_z tertiary motion amplitudes in X, Y and Z directions
DOC depth-of-cut
δ dimple phase shift distance
ε fraction part of the cutting frequency ratio
η elastic/plastic deformation ratio
f tool vibration frequency
$feed$ feed rate
G_α plane-setting angle
H_α elevation-setting angle
h vertical shift of the tool from the centerline
K integer part of the cutting frequency ratio
L_α roll-setting angle
L_0 initial tool position in the feed direction
$\hat{L}_{wk}, \hat{\rho}_{wk}, \hat{\theta}_{wk}$ tool coordinates in the workpiece frame
$\tilde{L}_{wk}, \tilde{\theta}_{wk}$ discretized tool coordinates
l_{cut} dimple distance in the cutting direction
λ cutting frequency ratio
N workpiece rotation speed (RPM)
N_t vibration sampling points
$O_t X_{th} Y_{th} Z_{th}$ tool-in-hand coordinate system

$O_t X_{tm} Y_{tm} Z_{tm}$ tool-in-machine coordinate system
$O_m X_m Y_m Z_m$ machine coordinate system
p_e elastic recovery rate (workpiece/cutting edge)
p_{ve} elastic recovery rate (workpiece/tool faces)
$\varphi_x, \varphi_y, \varphi_z$ tertiary motion phase shifts in X, Y and Z directions
R_0 workpiece radius
R_n tool nose radius
$\mathbf{R}_x, \mathbf{R}_y, \mathbf{R}_z$ homogenous rotation matrices
r_v interference length between the tool faces and the workpiece
r_{ve} elastic deformation limit (workpiece/tool faces)
ρ radial coordinate in the cylindrical frame
$\mathbf{T}$ homogenous translation matrix
t_c chip thickness
t_{ce} elastic deformation limit (workpiece/cutting edge)
t_{cmin} minimum chip thickness
t_{cmax} limit chip thickness for elastoplastic deformation
W dimple width
ω_s angular velocity of the workpiece rotation
ω_t angular velocity of the tool vibration
X_{init} tool initial radial position
ζ spatial resolution of the simulation

the cutting direction offers numerous possibilities for more complex texture shapes and patterns. It also brings the benefits of vibration assisted machining into the texturing process, which could also lead to the texturing of brittle materials.

The key component of the process is the tertiary motion generator (TMG) which produces an elliptical trajectory at the tool tip. Many attempts have been dedicated to the development of high performance transducers that deliver elliptical motion.
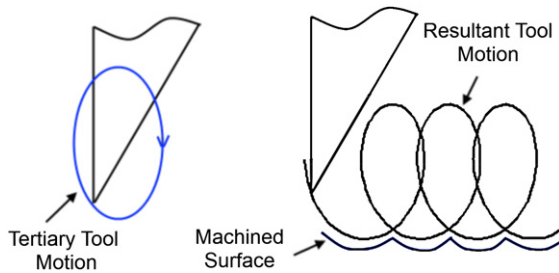

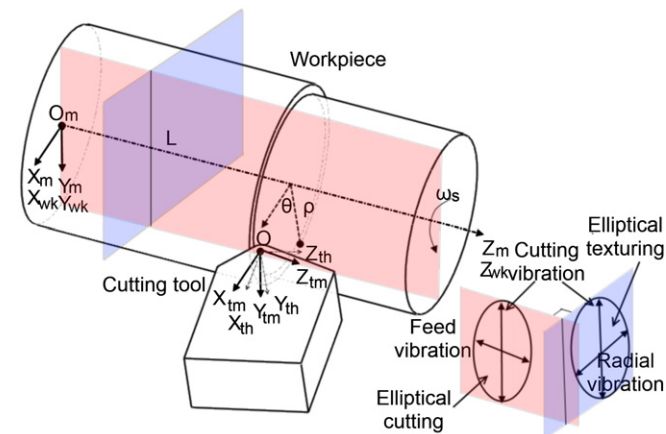**Fig. 1.** Schematic of the elliptical vibration texturing process.

Among them, Moriwaki and Shamoto's design [7] was the first attempt to incorporate a resonant piezo actuator in elliptical vibration cutting. Notable works also include Brinksmeier and Glabe's [10], Li et al.'s [11], and a commercial device EL-50 from Taga Eletric co., Ltd. [12] in the elliptical vibration cutting application. In the research area of ultrasonic motors, Kurosawa et al. [13] developed a V-shaped ultrasonic transducer, which can produce large vibration amplitudes in a compact size. Later Zhang et al. [14] developed a similar device based on Kurosawa's concept. Asumi et al. [15] further miniaturized this design.

A novel TMG developed by the authors is based on Kurosawa's idea, and is optimized for the elliptical texturing process. The device is working in the resonant mode in the ultrasonic frequency range. The cross-sectional view of the design is shown in Fig. 3. Details on the operating principle and the design of the TMG along with its performance assessment are given in [16].

There are many approaches for the prediction of surface generation in turning. Hong and Ehmann [17,18] proposed a generalized model of the surface generation process, which could include the tertiary motion of the cutting tool. Cheung et al. [19] and Kim et al. [20] developed simulation models for face turning through ultra-precision diamond turning and discussed the tool
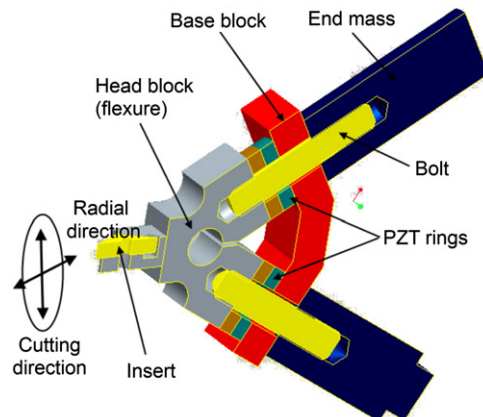

Fig. 2. Illustration of the elliptical cutting and elliptical texturing processes.

Fig. 3. Design of the resonant-mode tertiary motion generator (TMG).

vibration effect on the surface topography. Lin et al. [21] established a simulation model for the cylindrical turning operation. All these previous efforts cannot be directly applied to the elliptical vibration texturing process, for the following reasons: (1) all of them only include the cutting edge in the simulation, while in the elliptical vibration texturing process, the tool face and flank all contribute to shaping the final machined surface due to the tool's vibration; (2) many of the studies focus on the resultant surface roughness, while, in the current study, the detailed 3D topography of the machined surface is of greater interest; (3) previous works do not consider the cutting edge radius, elastic recovery, minimum chip thickness, etc., which play an important part in the micro-cutting mechanics. In the case of elliptical vibration texturing, it is imperative to incorporate these micro-cutting effects, since the vibration of the tool periodically changes the cutting depth from zero to the maximum depth, and the depth of the micro-features has a magnitude of several microns. Liu et al. [22] proposed a surface generation model for micro-end-milling, which is one of the few attempts in the literature to include the minimum chip thickness concept into the simulation of the surface generation process.

The objective of this paper is to study the surface generation mechanics of the elliptical vibration texturing process through experimentation and modeling. A surface generation model is developed to simulate the process. This generic surface simulation model focuses on the unique feature of the process: the high frequency and high amplitude vibrations between the tool and the workpiece, and models the process in the micro-cutting context. The structure of the paper is organized as follows. The surface generation model is first introduced in Section 2 followed by experimental verification in Section 3. The process analysis based on the simulations is discussed in Section 4, while conclusions are provided in Section 5.

2. Surface generation model

When the elliptical vibration texturing process is applied to cylindrical turning, the tertiary motion of the cutting tool causes complex interactions between the cutting tool and the workpiece. The vibration in the cutting direction periodically changes the cutting speed. The vibration in the radial direction changes the depth-of-cut. This is the driving factor for the generation of the texture. The terms, tertiary motion and tool vibration will be used interchangeably in this paper when referring to the periodic motion of the cutting tool. The cutting tool geometry determines the dimple (texture) shape. Besides, not only the cutting edge generates the surface (as often is the case in the conventional single-point diamond turning process), but the rake and flank faces of the cutting tool also play important roles in shaping the final surface features. For example, the clearance angle may change to a large negative value due to the vibration of the tool, which results in a large interference volume between the flank face and the workpiece. The ploughing effect on the surface topography induced by the tool faces should be considered in the simulation.

In this process, since the depth-of-cut approaches or actually is of the same scale as the cutting edge radius, the radius of the cutting tool can no longer be ignored. This changes the fundamental material removal mechanism from the shear dominant to the ploughing dominant regime. When the depth-of-cut decreases even further, there is a point where no chip will form [23]. This is known as the minimum chip thickness effect. The elastic recovery of the material is also not negligible when the depth-of-cut is comparable to the cutting edge radius. When the actual cutting depth is smaller than the minimal cutting depth all these effects influence the final surface topography. In the simulation model suitable provisions should be made to account for these cutting edge radius induced effects.

The overall surface generation algorithm is illustrated in Fig. 4. The approach taken is to first describe the 3D tool geometry, including its rake and flank faces and the cutting edge. The tertiary motions of the cutting tool are generalized and decomposed into three harmonic vibratory motions with different amplitudes and phases in three orthogonal directions. The cutting tool coordinates with the tertiary motion are now all time-varying parametric functions, which, through a series of homogenous transformations, are then expressed in the workpiece
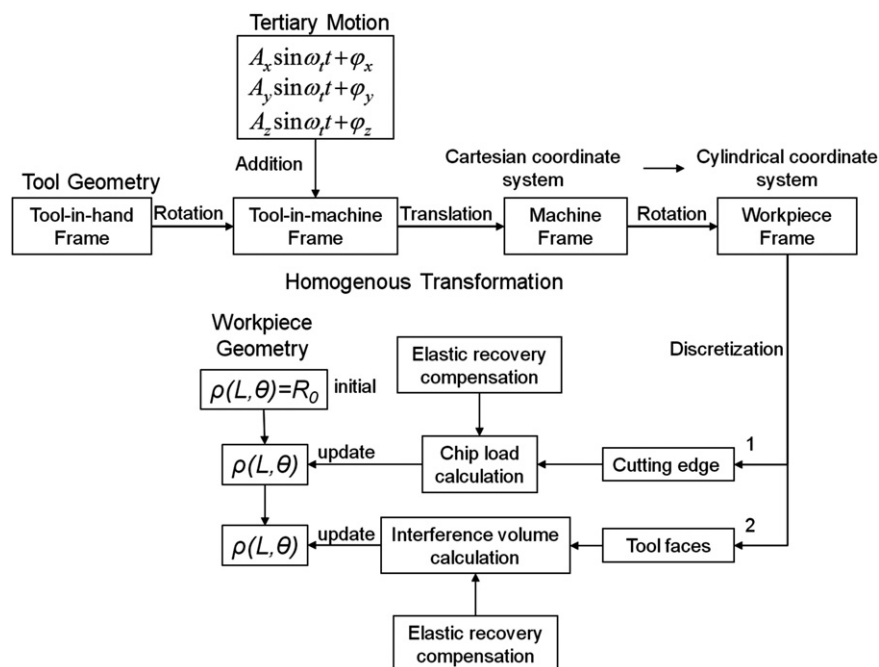

Fig. 4. Flow chart of the surface generation simulation.

coordinate system. The workpiece geometry (a cylinder in the turning operation) is stored in the form of mesh grids, which are discretized in the axial and azimuthal coordinates and remain continuous in the radial direction. During each simulation time step, the workpiece topography is updated in two steps: (1) the instantaneous chip thickness is first calculated in accordance with the current/instantaneous cutting edge coordinates. The actual cutting depth is derived/compensated considering the elastoplastic deformation and the minimum chip thickness effects. The workpiece mesh points are updated with the compensated cutting edge positions; and (2) the ploughing process induced by the tool faces is then considered. The tool faces' interference volume with the workpiece is calculated and adjusted for the elastoplastic deformation. The workpiece mesh points are updated again based on the adjusted interference volume. Special considerations are taken into account to handle the coordinate discretization and time step calculations.

The surface generation model is discussed in detail next, following the logic in Fig. 4. The tool geometry is described in the tool-in-hand coordinate system in Section 2.1. The relations and transformations between four different coordinate systems are discussed in Section 2.2. In Section 2.3, the tertiary motion of the tool is defined in the tool-in-machine frame. The discretization method is introduced in Section 2.4. Finally, in Sections 2.5 and 2.6, the two-step updating algorithm is discussed for the cutting edge effect and the ploughing process of the tool faces, respectively.

2.1. Description of tool geometry

According to the definition in [17], the cutting edge of the tool can be defined as the intersection of the tool rake and flank faces. A similar approach is taken here, so that the cutting tool geometry can be described by two parametric surface functions, which represent the tool face and flank. With a proper definition of boundary conditions for these two parametric functions, part of their boundary (a space curve) should coincide with each other, which corresponds to the tool cutting edge. The cutting edge is then indirectly included in this description, along with the tool rake and flank faces.

To simplify the expressions and to more clearly highlight the procedure, a special case corresponding to commercially available indexable inserts, shown in Fig. 5, will be used to introduce the generic tool geometry description method. The following three assumptions are made to simplify the model:

- The cutting tool has a nose radius R_n. The cutting depth is smaller than the nose radius (in the present case, a diamond insert with a 200 μm nose radius and a cutting depth less than 20 μm will be used).
- The rake face of the tool is a simple planar surface. The flank face keeps a constant clearance angle.
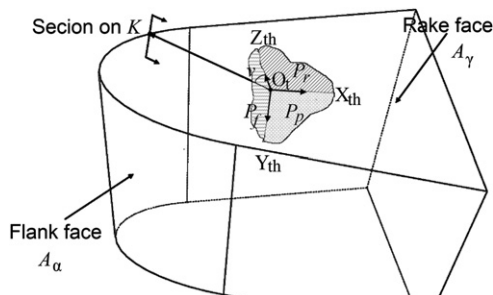- For simplicity, the cutting tool geometry is radially symmetrical.

Fig. 5. Cutting insert geometry definition.

These assumptions are only specific to the above-assumed example (a standard turning insert geometry). Different assumptions can be made for different tool geometries. With the above assumptions, the tool-in-hand coordinate system $(O_t X_{th} Y_{th} Z_{th})$ can be defined. The 3D tool geometry can be fully described in this coordinate system by a set of parametric functions:

$$X_{th}(u,v) = \begin{cases} -(R_n + u) \times \sin v & u \leq 0 \\ -(R_n - u \times \sin\alpha) \times \sin v & u > 0 \end{cases}$$

$$Y_{th}(u,v) = \begin{cases} 0 & u \leq 0 \\ u \times \cos\alpha & u > 0 \end{cases}$$

$$Z_{th}(u,v) = \begin{cases} (R_n + u) \times \cos v & u \leq 0 \\ (R_n - u \times \sin\alpha) \times \cos v & u > 0 \end{cases} \tag{1}$$

The parameter v denotes the angle between KO_t and the Z_{th} axis in the figure. The parameter u indicates the different parts of the tool. When $u > 0$, the parametric functions describe the flank face; when $u < 0$, the parametric functions describe the rake face. The cutting edge is included in the functions. When $u = 0$, the functions are reduced to a space curve, which denotes points on the cutting edge.

2.2. Description of the coordinate systems

The cylindrical turning scheme is shown in Fig. 2. There are four coordinate systems defined in the figure. The machine coordinate system $(O_m X_m Y_m Z_m)$ is defined according to convention [24]. The workpiece coordinate system $(O_m X_{wk} Y_{wk} Z_{wk})$ is attached to the workpiece, rotating around the Z_{wk} axis at a constant speed ω_s. It coincides with the machine coordinate system at the initial time instant. The tool-in-hand coordinate system $(O_t X_{th} Y_{th} Z_{th})$ is established on the tool rake face. The tool geometry is described in this coordinate system. The tool-in-machine coordinate system $(O_t X_{tm} Y_{tm} Z_{tm})$ is introduced to define the tool position and orientation in the machine tool system. The tool-in-machine coordinate system can be obtained by a pure translation transformation from the machine frame, and a pure rotation transformation from the tool-in-hand frame. Then, by a series of homogenous transformations, the cutting tool coordinates can be transformed from the tool-in-hand coordinate system to the workpiece coordinate system.

The relation between the tool-in-machine and tool-in-hand coordinate systems is a pure rotation transformation. Three setting angles G_α, H_α, L_α are defined according to convention [24]. These three angles define three rotation transformation matrices: $\mathbf{R}_x(-L_\alpha)$, $\mathbf{R}_y(-G_\alpha)$, and $\mathbf{R}_z(-H_\alpha)$.

The transformation between the machine and the tool-in-machine coordinate systems is a pure translation, which defines the translation matrix $\mathbf{T}(X_{init} - DOC, h, L_0 - feed \times t)$. X_{init} is the initial "touch" position; DOC stands for the nominal depth-of-cut; h is the vertical shift from the centerline of the cutting tool; L_0 is the initial tool position in the feed direction; $feed$ is the feed rate.

Another homogenous rotation matrix is needed to define the transformation from the machine coordinate system to the workpiece coordinate system. The transformation matrix is designated as $\mathbf{R}_z(-\omega_s \times t)$, where ω_s is the workpiece rotation speed. The rotation angle is zero at the initial time, and increases with time.

There are totally five homogenous transformations defined above that convert the tool coordinates from the tool-in-hand coordinate system to the workpiece coordinate system. Thus the cutting tool coordinates can be described in the workpiece frame

at any time instance by:

$$\begin{bmatrix} X_{wk}(u,v,t) \\ Y_{wk}(u,v,t) \\ Z_{wk}(u,v,t) \\ 1 \end{bmatrix} = \mathbf{R}_z(-\omega_s t) \cdot \mathbf{T}(X_{\mathrm{init}}-DOC, h, L_0-feed \times t) \cdot \mathbf{R}_x(-L_\alpha)$$

$$\cdot \mathbf{R}_y(-G_\alpha) \cdot \mathbf{R}_z(-H_\alpha) \cdot \begin{bmatrix} X_{th}(u,v) \\ Y_{th}(u,v) \\ Z_{th}(u,v) \\ 1 \end{bmatrix}$$

$$= \begin{bmatrix} \cos\omega_s t & \sin\omega_s t & 0 & 0 \\ -\sin\omega_s t & \cos\omega_s t & 0 & 0 \\ 0 & 0 & 1 & 0 \\ 0 & 0 & 0 & 1 \end{bmatrix}$$

$$\cdot \begin{bmatrix} 1 & 0 & 0 & X_{\mathrm{init}}-DOC \\ 0 & 1 & 0 & h \\ 0 & 0 & 1 & L_0-feed \times t \\ 0 & 0 & 0 & 1 \end{bmatrix}$$

$$\cdot \begin{bmatrix} 1 & 0 & 0 & 0 \\ 0 & \cos L_\alpha & \sin L_\alpha & 0 \\ 0 & -\sin L_\alpha & \cos L_\alpha & 0 \\ 0 & 0 & 0 & 1 \end{bmatrix}$$

$$\cdot \begin{bmatrix} \cos G_\alpha & 0 & -\sin G_\alpha & 0 \\ 0 & 1 & 0 & 0 \\ \sin G_\alpha & 0 & \cos G_\alpha & 0 \\ 0 & 0 & 0 & 1 \end{bmatrix}$$

$$\cdot \begin{bmatrix} \cos H_\alpha & \sin H_\alpha & 0 & 0 \\ -\sin H_\alpha & \cos H_\alpha & 0 & 0 \\ 0 & 0 & 1 & 0 \\ 0 & 0 & 0 & 1 \end{bmatrix} \cdot \begin{bmatrix} X_{th}(u,v) \\ Y_{th}(u,v) \\ Z_{th}(u,v) \\ 1 \end{bmatrix} \quad (2)$$

2.3. Description of the tertiary motion

The vibration of the tool tip is the higher order/tertiary motion. The trajectory of the tool tip is generally an elliptical curve in 3D space. It is defined in the tool-in-machine frame. The projections of the trajectory onto the three base axes (X_{tm}, Y_{tm} and Z_{tm}) are three sinusoidal functions with the same angular velocity ω_t, but with different amplitudes and phase shifts. They are designated as A_x, A_y, A_z, φ_x, φ_y, φ_z, respectively. Similar homogenous transformations are applied to the tertiary motion to transform the coordinates to the workpiece frame. Consequently, the tool coordinates with the tertiary motion in the workpiece coordinate system can be written as:

$$\begin{bmatrix} \hat{X}_{wk}(u,v,t) \\ \hat{Y}_{wk}(u,v,t) \\ \hat{Z}_{wk}(u,v,t) \\ 1 \end{bmatrix} = \mathbf{R}_z(-\omega_s t) \cdot \mathbf{T}$$

$$\cdot \left\{ \mathbf{R}_x \cdot \mathbf{R}_y \cdot \mathbf{R}_z \cdot \begin{bmatrix} X_{th}(u,v) \\ Y_{th}(u,v) \\ Z_{th}(u,v) \\ 1 \end{bmatrix} + \begin{bmatrix} A_x \sin\omega_t t + \varphi_x \\ A_y \sin\omega_t t + \varphi_y \\ A_z \sin\omega_t t + \varphi_z \\ 0 \end{bmatrix} \right\} \quad (3)$$

It is appropriate to express the cutting tool coordinates with the tertiary motion in the cylindrical form (workpiece frame) for

faster calculation. The expressions are given by:

$$\begin{bmatrix} \hat{L}_{wk}(u,v,t) \\ \hat{\rho}_{wk}(u,v,t) \\ \hat{\theta}_{wk}(u,v,t) \end{bmatrix} = \begin{bmatrix} \hat{Z}_{wk}(u,v,t) \\ \|\hat{X}_{wk}(u,v,t)+\boldsymbol{i}\hat{Y}_{wk}(u,v,t)\| \\ \arg\{\hat{X}_{wk}(u,v,t)+\boldsymbol{i}\hat{Y}_{wk}(u,v,t)\} \end{bmatrix} \quad (4)$$

2.4. Space and time discretization

Both space and time are discretized for the computer simulations. Mesh grids are assigned to the workpiece and the cutting tool. The interval of the mesh grids is determined by the desired spatial resolution, ζ, of the simulation. The angular resolution is determined accordingly by the ratio of the spatial resolution over the radius. For the workpiece expression $\rho(L,\theta) = R_0$, the length L and azimuth θ are discretized to the specific spatial and angular resolutions (ζ and ζ/R_0), while the radial distance component ρ is continuous. Similarly, for the cutting tool, the parametric variables u and v are discretized accordingly.

The time step is determined by three motions: the cutting motion, the feed motion, and the tertiary motion of the tool. The goal is to restrict the tool motion to a comparable magnitude to the spatial resolution during each time step. The feed motion velocity is much smaller than the other two determining factors. The cutting speed and the maximal vibration speed of the tool are of comparable order. So the time step takes the value which is inversely proportional to either the cutting speed or the maximal vibration speed. The mathematical relation is given by:

$$t_{\mathrm{timestep}} = \min\left\{ \frac{\zeta}{R_o \times \omega_s}, \frac{2\pi}{N_t \omega_t} \right\} \quad (5)$$

where ω_s is the spindle rotation velocity (cutting speed); ζ/R_0 is the angular resolution of the simulation; N_t represents the sampling points on the tool vibration trajectory, which determines how smooth the tool vibration motion is captured in the simulation.

In each time step, the trajectory of the cutting tool is updated in the workpiece frame according to Eq. (4). The azimuth and length coordinates, $\hat{\theta}_{wk}(u,v,t)$ and $\hat{L}_{wk}(u,v,t)$, are rounded to the nearest workpiece mesh points in accordance with:

$$\tilde{L}_{wk}(u,v,t) = \left\lceil \frac{\hat{L}_{wk}(u,v,t)}{\zeta} \right\rceil$$

$$\tilde{\theta}_{wk}(u,v,t) = \left\lceil \frac{\mathrm{mod}(\hat{\theta}_{wk}(u,v,t),2\pi) \times R_0}{\zeta} \right\rceil \quad (6)$$

2.5. Workpiece update with the cutting edge effect

At each time step, the vector set $[\hat{L}_{wk}(u,v,t),\hat{\rho}_{wk}(u,v,t),\hat{\theta}_{wk}(u,v,t)]^{\mathrm{T}}$, describing the current tool coordinates with respect to the workpiece frame in the cylindrical form, contains both the cutting edge and tool faces. The cutting edge points $[\hat{L}_{wk}(0,v,t),\hat{\rho}_{wk}(0,v,t),\hat{\theta}_{wk}(0,v,t)]^{\mathrm{T}}$ alone are obtained by setting the parametric variable $u=0$. After discretization of the length and azimuth components according to Eq. (6), the cutting edge points are aligned to the nearest workpiece grid points. For any point on the cutting edge (a given parameter value v) that intersects with the workpiece, the instantaneous chip thickness is calculated as:

$$t_c^v = \rho(\tilde{L}_{wk}(0,v,t),\tilde{\theta}_{wk}(0,v,t)) - \hat{\rho}_{wk}(0,v,t) \quad (7)$$

The schematic of the calculation is illustrated in Fig. 6. The chipload is represented by the area with vertical lines. For a point v on the cutting edge, the instantaneous chip thickness is
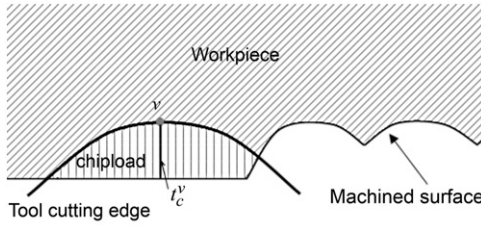
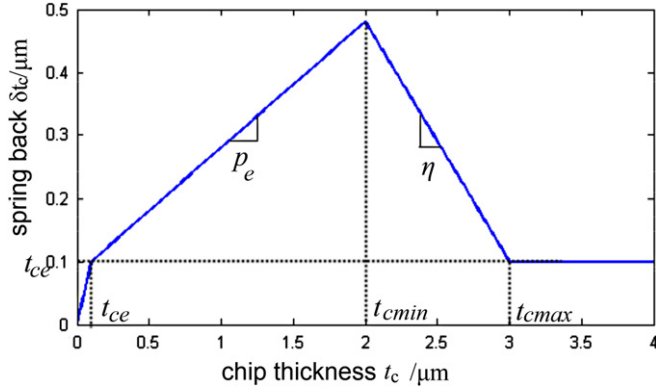Fig. 6. Instantaneous chip thickness calculation.

Fig. 7. Elastic recovery function of the chip thickness.

approximated as the difference between the corresponding workpiece radius and the radial coordinate of point v.

The expression for the springback amount δt_c of the material is modified from Liu et al.'s work [22]. In [22], the springback amount is assumed to be zero when the chip thickness exceeds the minimum chip thickness. In this paper, a more feasible assumption is made, namely, it is assumed that when the chip thickness is greater than the minimum chip thickness the elastic recovery still exists and linearly decreases to a constant value, which is a process constant related to the tool edge radius, and the material hardness and elastic modulus [25]. The springback amount function is than established to be a piecewise function of the chip thickness t_c and is continuous over the whole range. It is given by:

$$\delta t_c = \begin{cases} t_c & t_c < t_{ce} \\ p_e(t_c - t_{ce}) + t_{ce} & t_{ce} \leq t_c < t_{cmin} \\ \eta(t_{cmax} - t_c) + t_{ce} & t_{cmin} \leq t_c < t_{cmax} \\ t_{ce} & t_c \geq t_{cmax} \end{cases} \quad (8)$$

where t_{ce} is the elastic deformation limit; t_{cmin} is the minimum chip thickness; t_{cmax} is the limit chip thickness for elastoplastic deformation; p_e is the elastic recovery rate of the workpiece when the cutting chip thickness is smaller than the minimum chip thickness, which is a process constant that depends on the tool edge radius, material properties, etc.; η is the elastic/plastic deformation ratio when the chip load is greater than the minimum chip thickness. η is a dependent variable to ensure the continuity of the function. The expression is given by:

$$\eta = \frac{p_e(t_{cmin} - t_{ce})}{t_{cmax} - t_{cmin}} \quad (9)$$

The plot of the springback function is shown in Fig. 7. When the chip thickness t_c is smaller than the elastic deformation limit t_{ce}, the workpiece material is fully recovered with no plastic deformation. The slope of the function is one. When t_c is between the elastic deformation limit and the minimum chip thickness t_{cmin}, no chip will form. The cutting process turns into a pure

ploughing process. The material undergoes elastoplastic deformation. The elastic recovery rate p_e is the slope of the function in this range. When t_c reaches the minimum chip thickness, the materials have the maximum springback amount. When t_c passes the minimum chip thickness value, the material removal mechanism changes into a shear/ploughing combined process, until t_c reaches t_{cmax}, where it becomes a shear dominant process. η is the slope of the function when it is defined between t_{cmin} and t_{cmax}. When t_c is greater than t_{cmax}, the elastic recovery amount remains a constant value which is equal to t_{ce}, the elastic deformation limit.

Then, the radius of the workpiece corresponding to the cutting edge point, v, is updated with the calculated chip thickness and elastic recovery. The new radial coordinates are updated in the workpiece mesh arrays in accordance with:

$$\rho(\tilde{L}_{wk}(0,v,t), \tilde{\theta}_{wk}(0,v,t)) = \hat{\rho}_{wk}(0,v,t) + \delta t_c^v \quad (10)$$

2.6. Workpiece update with the ploughing effect from the tool faces

The tool face coordinates are described by the vector set $[\hat{L}_{wk}(u,v,t), \hat{\rho}_{wk}(u,v,t), \hat{\theta}_{wk}(u,v,t)]^T$, when $u \neq 0$. They contact the workpiece during the texturing process due to the tertiary motion of the tool. They also contribute to the final shape of the machined surface. Their interaction with the workpiece is modeled as a ploughing process, which plastically deforms the material. At each time step, the workpiece coordinates are first updated for the cutting edge effect described in the previous section. Then, the interference volume of the cutting tool and workpiece is calculated based on the coordinates of the tool faces. The interference volume is discretized and evaluated at each grid points on the tool faces. At any point (u,v) on the tool faces, the unit interference volume is calculated as the radial coordinate difference between the tool face point (u,v) and the corresponding workpiece grid point as:

$$r_v^{u,v} = \rho(\tilde{L}_{wk}(u,v,t), \tilde{\theta}_{wk}(u,v,t)) - \hat{\rho}_{wk}(u,v,t) \quad u \neq 0 \quad (11)$$

The springback amount is calculated similarly for the ploughing process, and is given by:

$$\delta r_v = \begin{cases} r_v & r_v < r_{ve} \\ p_{ve}(r_v - r_{ve}) + r_{ve} & r_v \geq r_{ve} \end{cases} \quad (12)$$

where r_{ve} is the elastic deformation limit; p_{ve} is the elastic recovery rate of the workpiece for the ploughing process between the tool faces and the workpiece.

Finally, the workpiece coordinates are updated again for the ploughing process induced by the tool faces:

$$\rho(\tilde{L}_{wk}(u,v,t), \tilde{\theta}_{wk}(u,v,t)) = \hat{\rho}_{wk}(u,v,t) + \delta r_v^{u,v} \quad u \neq 0 \quad (13)$$

3. Experimental verification

The tertiary motion generator (TMG) that is used for the verification of the simulation models works in the resonant mode at 28 kHz. The motion of the tool tip is monitored by MicroSense capacitance sensors, which have a sub-nanometer resolution and a 100 kHz bandwidth. The measured trajectories are plotted in Fig. 8. The vibration amplitudes are around 4 μm in both directions and the phase shift is 41°.

The newly developed TMG was integrated into a desktop turning/milling/drilling machine. The X–Y stage carries the TMG and has a resolution of 0.25 μm in both directions. The Z axis supports a high speed air spindle and a linear stage with a 1.27 μm resolution. The machine is configured to operate as

vertical lathe. The workpiece is loaded in the spindle along the Z axis. The spindle provides the primary motion for the turning operation. The linear motor in the Z axis controls the feed motion. The X–Y stage sets the depth of cut. A special rotary fixture was designed to change the orientation of the TMG.

A series of experiments were conducted to compare the results with the simulations. Different combinations of process parameters, workpiece materials and tool geometry were used in the experiments. The workpiece materials used were aluminum 6061 and copper 110. Due to the focus of the paper, only ductile materials were used for easy verification of the simulation model. The workpiece had a diameter of 3 mm (1/8 in.). Two kinds of cutting inserts were used: a carbide insert with a 0° rake angle, 7° clearance angle and a 400 μm nose radius, and a diamond insert

with the same specs but a 200 μm nose radius. The machined surface was examined under a Zygo white light interferometer.

The input parameters for the simulation were kept the same as the experimental conditions. Namely, the original radius of the workpiece R_0 was set to 1500 μm. The tertiary motion semi-amplitudes were set to 2 μm for A_x, 2 μm for A_y, and 0 for A_z. The phase angles were set accordingly to 41° for φ_x, and 0° for φ_y and φ_z. The tool nose radius value R_n was set to 200 μm. The vibration frequency f was 28 kHz. The spindle rotation speed N, the feed rate feed, and the cutting depth DOC were determined according to each individual experiment, which is discussed in the following paragraph. There are certain other process and material related constants needed for the simulation, such as the elastic recovery rate, spatial resolution for the simulation, etc. In the current study, the following parameter values were used: the setting angles G_α, H_α, L_α were all set to 0°; the spatial resolution $\zeta = 1$ μm; the vibration sampling frequency $N_t = 80$; the elastic deformation limits t_{ce} and r_{ve} were taken as 0.01 μm and 0.1 μm; the minimum chip thickness $t_{cmin} = 0.04$ μm; the elastic recovery rates p_e and p_{ve} were 0.1 and 0.5, respectively; the limit chip thickness $t_{cmax} = 0.1$ μm; and the elastic/plastic deformation ratio η was calculated to be 0.05. The cutting edge radius for the diamond tool is assumed to be 100 nm. The minimum chip thickness to edge radius ratio is taken as 0.40 [10]. These assumptions yield a minimum chip thickness value of 40 nm.

One example of the experimental results is plotted in Fig. 9(a). The comparable simulation results are illustrated in Fig. 9(b). In this example, the workpiece material is aluminum 6061; the cutting insert used is the diamond insert with the 200 μm nose radius. The workpiece was first pre-turned without the vibrations using the same diamond tool. Then the workpiece was textured with the tertiary motion of the cutting tool. The spindle speed was set around 7500 rpm and the feed rate was set at 60 μm/rev. The input parameters for the simulation were described above. The turning speed was set to be 7517 rpm, which affects the dimple patterns. Another example for comparison is plotted in Fig. 10. In the second
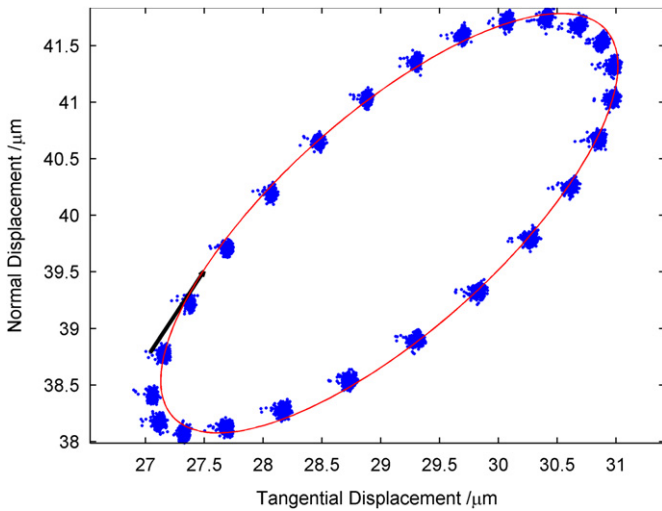

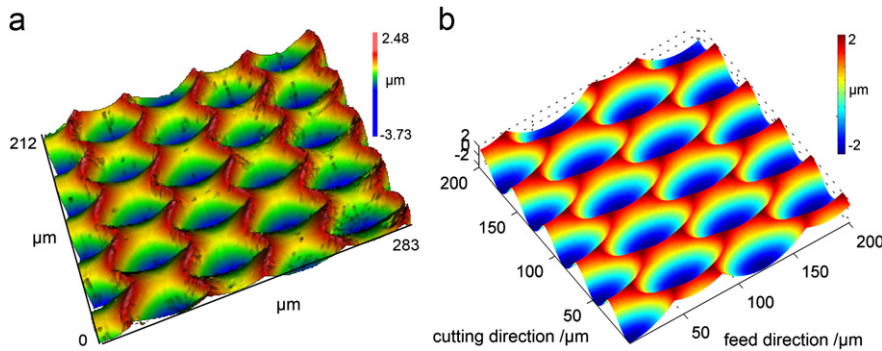Fig. 8. Tool vibration trajectory.

Fig. 9. Surface topography (set 1): (a) experimental results; (b) simulation results.
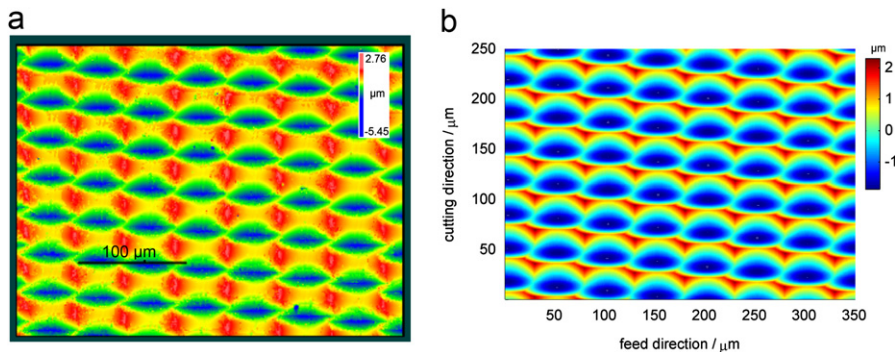

Fig. 10. Surface topography (set 2): (a) experimental results; (b) simulation results.

example, the same workpiece material and cutting insert were used. The spindle speed and the feed rate were changed to ~6000 rpm and 50 μm/rev, respectively. The actual spindle speed input to the simulation was 5997 rpm. All the experimental and simulation conditions are summarized in Table 1.

From the comparison, the simulated topography is very similar to the experimental results. The simulation successfully captures the surface features, such as the dimple shapes and patterns. The sets of experimental results confirm the validity of the simulation. One example of the surface profile comparison along

Table 1
Experimental conditions.

| *Cutter geometry*			
Style	DCMW	Material	Diamond
Rake angle	0	Nose radius	200 μm
Clearance angle	7°		
Tertiary motion			
Vibration frequency	28 kHz		
Radial direction amplitude	4 μm (peak-to-peak)		
Cutting direction amplitude	4 μm (peak-to-peak)		
Phase shift	41°		
Process parameter (Set 1)			
Texturing		Pre-turning	
Spindle speed	~7500 rpm	Spindle speed	~12,500 rpm
Feed rate	60 μm/rev	Feed rate	5 μm/rev
Nominal DOC	2 μm	Nominal DOC	10 μm
Process parameter (Set 2)			
Texturing		Pre-turning	
Spindle speed	~6000 rpm	Spindle speed	~12500 rpm
Feed rate	50 μm/rev	Feed rate	5 μm/rev
Nominal DOC	2 μm	Nominal DOC	10 μm
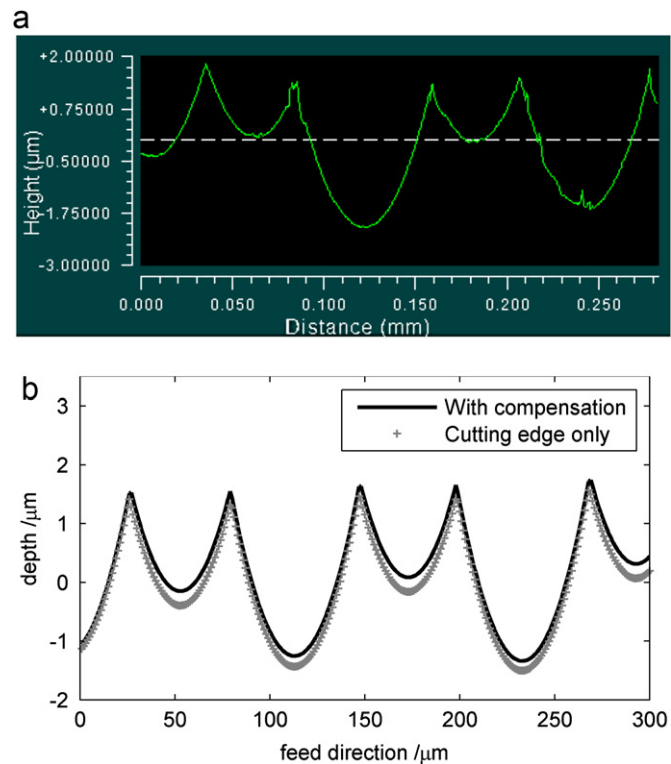
Fig. 11. Surface profile comparison along the feed direction: (a) measured results; (b) simulated results.
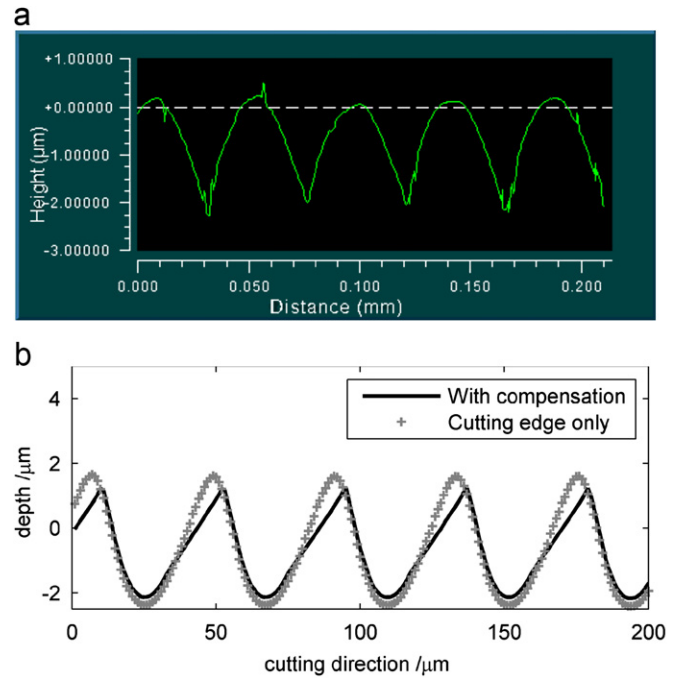
Fig. 12. Surface profile comparison along the cutting direction: (a) measured results; (b) simulated results.

the feed direction is shown in Fig. 11. The dotted line shows the simulated surface profile considering only the cutting edge (single point cutting simulation), while the solid line represents the surface profile with the ploughing effect and elastic recovery. The simulation correctly identifies the modulated profile feature. The surface profiles along the cutting direction are plotted and compared in Fig. 12. A similar comparison between the surface profiles with and without the compensation is also shown in Fig. 12(b). After a closer look at the measured surface profile, one can clearly see some discrepancy from the simulated results. This could arise from the ignored system dynamics. The tool vibration trajectory is measured without loads, while the actual vibration amplitudes might be reduced due to the cutting load. Moreover, other complex micro cutting mechanics beyond this simple elastic recovery compensation could affect the surface profile. The simulation results, nevertheless, are accurate in terms of the micro dimple arrangement and the overall surface topography. This surface generation program then can be used to analyze the effects of different process parameters, tool geometry, and tertiary motion on the textured surface. Since the TMG works in the resonant vibration mode, the vibration frequency, amplitudes and phases are fixed for the current design. This paper mainly focuses on the analysis of the influences of the process parameters and the tool geometry on the topography of the textured surfaces.

4. Effects of the process parameters

4.1. Cutting frequency ratio

The cutting speed in the elliptical vibration texturing process is no longer a constant value. It undergoes periodic variations due to the tertiary motion of the tool tip. The ratio of the spindle speed and the tool vibration frequency is a very important factor that determines the texture patterns. This ratio, λ, to be referred to as the "*cutting frequency ratio*", is defined as the vibration

frequency over the spindle rotation speed, i.e.:

$$\lambda = \frac{60f}{N} \qquad (14)$$

If the vibration of the cutting tool is assumed to be a rigid body movement, and only the primary motion is considered (no feed motion), the trajectory of any point on the tool tip can be expressed as:

$$X = A_x \sin(\omega_t t + \varphi_x) + \frac{\omega_t}{\lambda} R_0 t$$
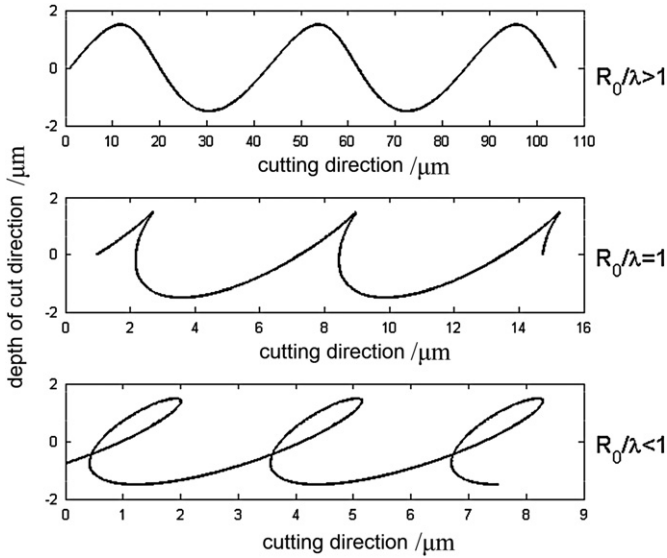
$$Y = A_y \sin(\omega_t t + \varphi_y) \qquad (15)$$

Fig. 13. Tool vibration trajectories.

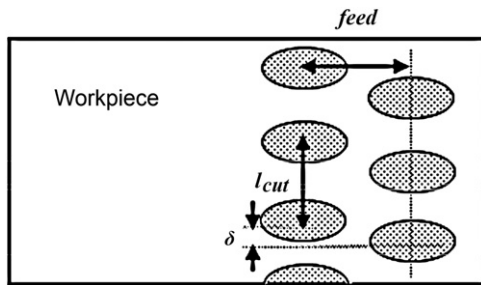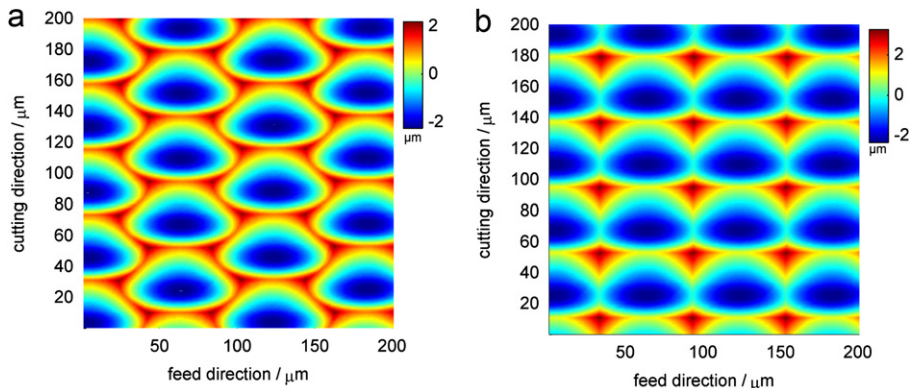Fig. 14. Texture pattern arrangement.

The value of the workpiece radius over the cutting frequency ratio R_0/λ separates the vibration trajectory into three categories that are illustrated in Fig. 13. The vibration amplitudes, frequency and phases are set to be the same as in Table 1. When $R_0/\lambda > 1$, the dimples do not intersect in the cutting direction and the cutting tool always moves forward relative to the workpiece. When $R_0/\lambda < 1$, there is a reverse movement of the cutting tool as shown in the figure. The dimples overlap with the successive ones. The condition $R_0/\lambda = 1$ separates the two regions and stagnation points appear on the trajectory (zero cutting speed).

Only when $R_0/\lambda \geq 1$, the gap distance between two neighboring dimples in the cutting direction can be defined as (Fig. 14):

$$l_{cut} = \frac{2\pi R_0}{\lambda} \qquad (16)$$

4.2. Phase shift

From the simulation results in Fig. 9 and Fig. 10, a phase shift between two consecutive columns of dimples can be noted. The phase shift distance, δ, is defined in Fig. 14. This distance is determined by the cutting frequency ratio, λ. The cutting frequency ratio can be separated into an integer part, K, and a fraction part, ε, and expressed as:

$$\lambda = \frac{60f}{N} = K + \varepsilon \qquad (17)$$

The integer K determines the number of dimples along the perimeter of the workpiece. The fraction part ε is the remainder, which characterizes the phase shift distance δ. If ε equals to zero, i.e., λ is an integer, dimples will be aligned in the feed direction as shown in Fig. 15(b). If ε is greater than zero, a phase shift distance, δ, is generated. The phase shift can be calculated from:

$$\delta = \frac{2\pi R_0 \varepsilon}{\lambda} \qquad (18)$$

An example of a simulated topography with a phase shift is plotted in Fig. 15(a), where the cutting frequency ratio λ is 223.49 and the phase shift distance δ is 20.81 μm.

4.3. Feed rate

The feed rate, *feed*, determines the dimple gap in the horizontal direction (feed direction), as shown in Fig. 14. When the feed rate is small enough, the dimples begin to overlap in the feed direction. This critical feed rate at which dimples start to overlap, however, depends on the tool geometry as well as other process parameters. If the dimple geometry is approximated as a diamond
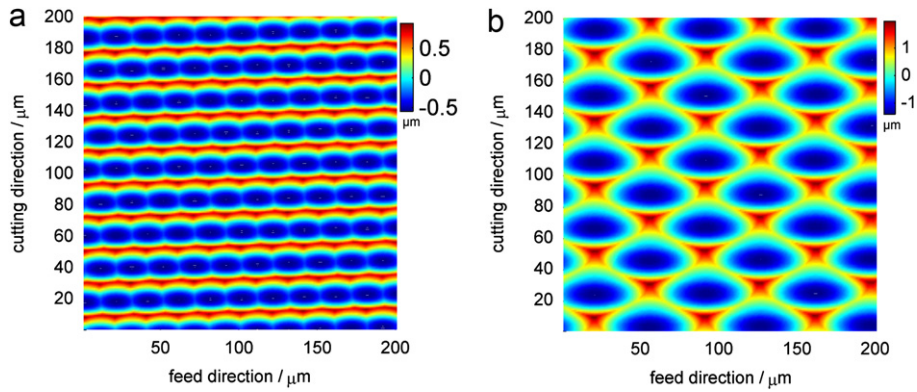

Fig. 15. Simulated surfaces with different fraction values (ε) in the cutting frequency ratio: (a) $\varepsilon \neq 0$ and (b) $\varepsilon = 0$.

Fig. 16. Simulated surfaces with different feed rates: (a) *feed*=10 μm/rev; (b) *feed*=35 μm/rev.
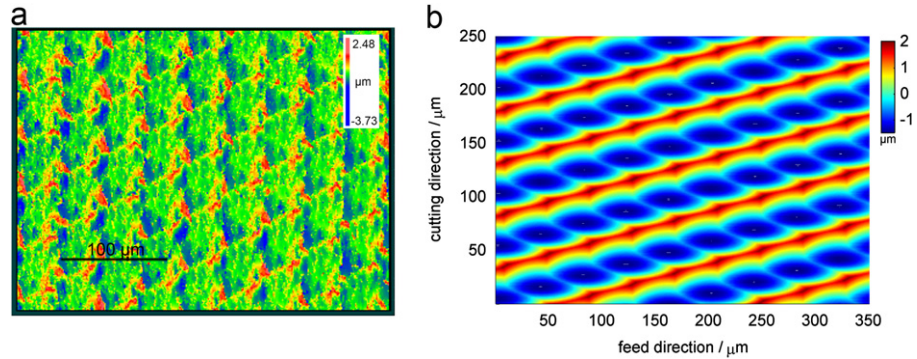

Fig. 17. Textured surfaces with the carbide tool: (a) experimental results; (b) simulation results.
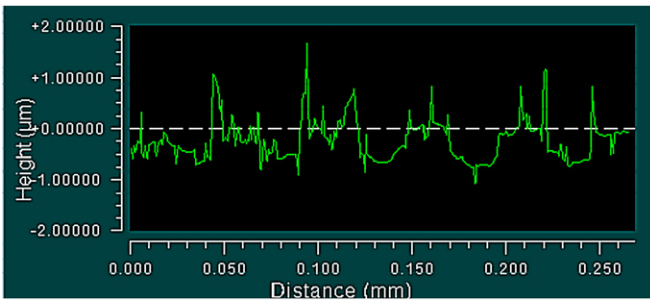

Fig. 18. Surface profile along the cutting direction with the carbide tool.

shape, the mathematical expression for the critical feed rate is:

$$feed_{critical} = W(1 - \frac{\delta}{l_{cut}}) \qquad (19)$$

where W is the dimple width; δ and l_{cut}, the phase shift and the gap distance in the cutting direction, are defined before.

Two examples of simulated topographies are shown in Fig. 16. The simulation inputs are kept the same as the first set of process parameters in Table 1, except for different feed rates. In Fig. 16(a), when the dimples intersect with each other in the feed direction, the overall feature of the textured surfaces dramatically changes and micro channels are formed. The case for the critical feed rate is shown in Fig. 16(b), in which the feed rate is calculated to be 35 μm.

5. Effects of the cutting tool

5.1. Tool materials

The cutting inserts used in the experiments were carbide inserts with a 400 μm and diamond inserts with a 200 μm nose radius.

The diamond inserts give much better results (Fig. 9(a) and Fig. 10(a)), in terms of better defined surface features, and match the simulation results very well. A textured surface generated by the carbide tool is shown in Fig. 17(a). The corresponding simulation results are shown in Fig. 17(b), for a spindle speed of 8760 rpm and a feed rate of 40 μm/rev.

The two figures in Fig. 17 share certain similarities; in general, however, the details of the dimple features are partially lost in the experimental results. This is due to the nature of the elliptical vibration texturing process. The cutting depth and width change periodically during the process. In many cases, the actual cutting depth is smaller or of the same order as the minimum chip thickness. When the depth-of-cut is nearly equal to the minimum chip thickness, the material removal mechanism changes from a shear dominant to a ploughing dominant process. The minimum chip thickness is closely related to the sharpness of the cutting tool. Its magnitude is around 0.3–0.5 of the edge radius.

In the cases of the carbide and diamond inserts, the diamond tool is much sharper than the carbide tool. The diamond tool usually has an edge radius on the order of tens of nanometers. The cutting depth of the elliptical vibration texturing process is still larger as compared to the diamond tool's cutting edge. Less elastic deformation and less ploughing take place in the case of the diamond insert, hence, better defined surface features can be achieved. For the carbide insert, the measured edge radius is around 40 μm. The cutting depth in this case is actually smaller than the edge radius. The ploughing is so severe that no stable cutting condition is established during the texturing process. This leads to the loss of detail in the generated texture and very bad surface finishes. The surface profile along the cutting direction, for example, is shown in Fig. 18. Large elastic deformations and recovery take place that leads to the deviations of the final shape from the simulation results even with spring-back compensation (the minimum chip thickness is set to 16 μm accordingly).
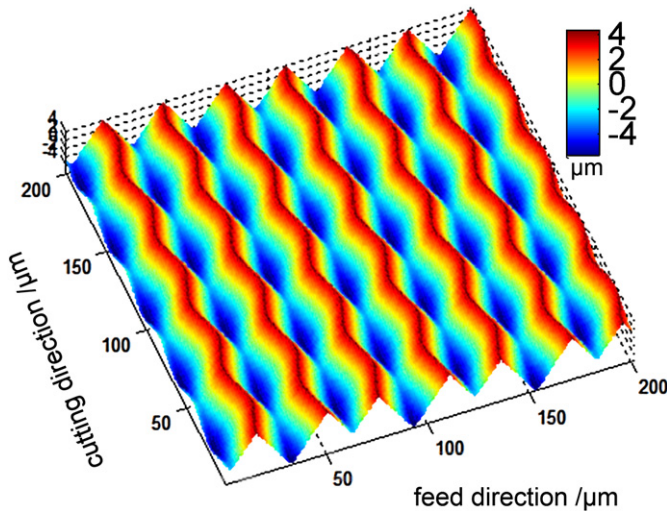
Fig. 19. Simulated surfaces with a triangular tool.

5.2. Tool geometry

The cutting geometry affects the shape of the dimples on the textured surface. In the current case, the cutting tool has a round front (Fig. 5). This generates simple dimple shapes on the workpiece surface. With different tool geometry, other interesting texture features can also be generated. One example of textured surfaces generated by a triangle-shaped cutting tool is shown in Fig. 19.

As for the round tool, the length of the dimples (length in the cutting direction) is mainly determined by the cutting frequency ratio, λ, but is also affected by the phase shift, δ. The width of the dimples (length in the feed direction) is determined by the nose radius of the cutting tool. If the ratio R_0/λ is assumed to be greater than one (top case in Fig. 13), the tool cuts into the workpiece by the peak-to-peak amplitude of the vibration ($2A_x$). The dimple width W is then calculated as:

$$W = 2\sqrt{R_n^2 - (R_n - 2A_x)^2} = 4\sqrt{R_n A_x + A_x^2} \qquad (20)$$

6. Conclusion

Based on the results and analysis in the present paper, the following conclusions can be drawn:

1. The proposed simulation algorithm includes a generic 3D tool geometry description method, which describes the tool's faces as parametric functions and includes the cutting edge points by restraining one parametric variable.
2. The simulation model takes into account the tool's tertiary motion and elastic recovery compensation considering the minimum chip thickness and ploughing effects.
3. The experimental results validate the feasibility of the surface generation model that can successfully simulate the detailed surface topography of the textured surface.
4. The tool geometry determines the texture shape, while the process parameters, namely the cutting speed and the feed rate, mainly determine the dimple patterns. Their influence on the phase shift and the dimple distance in the cutting and feed directions is discussed. The mathematical expressions are also given.
5. The elliptical vibration texturing process works in the micro-cutting regime. The ploughing effect plays an important role in

the material removal mechanism. The elastic recovery deteriorates the details of the textures. Sharp tools (diamond inserts) are preferred in this process, since they reduce the elastic deformation and ploughing effect.

Acknowledgement

References

[1] A. Kovalchenko, O. Ajayi, A. Erdemir, G. Fenske, I. Etsion, The effect of laser texturing of steel surfaces and speed-load parameters on the transition of lubrication regime from boundary to hydrodynamic, Tribology Transactions 47 (2004) 299–307.

[2] X.-M. Li, D. Reinhoudt, M. Crego-Calama, What do we need for a super-hydrophobic surface? A review on the recent progress in the preparation of superhydrophobic surfaces, Chemical Society Reviews 36 (2007) 1350–1368.

[3] A.A.G. Bruzzone, H.L. Costa, P.M. Lonardo, D.A. Lucca, Advances in engineered surfaces for functional performance, CIRP Annals—Manufacturing Technology 57 (2008) 750–769.

[4] T. Moriwaki, E. Shamoto, Ultraprecision diamond turning of stainless steel by applying ultrasonic vibration, CIRP Annals—Manufacturing Technology 40 (1991) 559–562.

[5] E. Shamoto, T. Moriwaki, Study on elliptical vibration cutting, CIRP Annals—Manufacturing Technology 43 (1994) 35–38.

[6] E. Shamoto, T. Moriwaki, Ultraprecision diamond cutting of hardened steel by applying elliptical vibration cutting, CIRP Annals—Manufacturing Technology 48 (1999) 441–444.

[7] T. Moriwaki, E. Shamoto, Ultrasonic elliptical vibration cutting, CIRP Annals—Manufacturing Technology 44 (1995) 31–34.

[8] C. Nath, M. Rahman, Effect of machining parameters in ultrasonic vibration cutting, International Journal of Machine Tools and Manufacture 48 (2008) 965–974.

[9] T. Moriwaki, E. Shamoto, K. Inoue, Ultraprecision ductile cutting of glass by applying ultrasonic vibration, CIRP Annals—Manufacturing Technology 41 (1992) 141–144.

[10] X. Liu, R.E. Devor, S.G. Kapoor, An analytical model for the prediction of minimum chip thickness in micromachining, American Society of Mechanical Engineers, New York, NY, ETATS-UNIS, 2006.

[11] X. Li, D. Zhang, Ultrasonic elliptical vibration transducer driven by single actuator and its application in precision cutting, Journal of Materials Processing Technology 180 (2006) 91–95.

[12] C. Nath, M. Rahman, K.S. Neo, A study on ultrasonic elliptical vibration cutting of tungsten carbide, Journal of Materials Processing Technology 209 (2009) 4459–4464.

[13] M. Kuribayashi Kurosawa, O. Kodaira, Y. Tsuchitoi, T. Higuchi, Transducer for high speed and large thrust ultrasonic linear motor using two sandwich-type vibrators, IEEE Transactions on Ultrasonics, Ferroelectrics, and Frequency Control 45 (1998) 1188–1195.

[14] F. Zhang, W. Chen, J. Lin, Z. Wang, Bidirectional linear ultrasonic motor using longitudinal vibrating transducers, IEEE Transactions on Ultrasonics, Ferro-electrics, and Frequency Control 52 (2005) 134–138.

[15] K. Asumi, R. Fukunaga, T. Fujimura, M.K. Kurosawa, Miniaturization of a v-shape transducer ultrasonic motor, Japanese Journal of Applied Physics 48 (2009).

[16] P. Guo, K.F. Ehmann, Development of a new vibrator for elliptical vibration texturing, ASME Conference Proceedings (2011) 373–380.

[17] K.F. Ehmann, M.S. Hong, A generalized model of the surface generation process in metal cutting, CIRP Annals—Manufacturing Technology 43 (1994) 483–486.

[18] M.S. Hong, K.F. Ehmann, Generation of engineered surfaces by the surface-shaping system, International Journal of Machine Tools and Manufacture 35 (1995) 1269–1290.

[19] C.F. Cheung, W.B. Lee, Modelling and simulation of surface topography in ultra-precision diamond turning, Proceedings of the Institution of Mechanical Engineers, Part B: Journal of Engineering Manufacture 214 (2000) 463–480.

[20] D.-S. Kim, I.-C. Chang, S.-W. Kim, Microscopic topographical analysis of tool vibration effects on diamond turned optical surfaces, Precision Engineering 26 (2002) 168–174.

[21] S.C. Lin, M.F. Chang, A study on the effects of vibrations on the surface finish using a surface topography simulation model for turning, International Journal of Machine Tools and Manufacture 38 (1998) 763–782.

[22] X. Liu, R.E. DeVor, S.G. Kapoor, Model-based analysis of the surface generation in microendmilling—Part I: Model development, Journal of Manufacturing Science and Engineering 129 (2007) 453–460.

[23] N. Ikawa, S. Shimada, H. Tanaka, Minimum thickness of cut in micromachining, Institute of Physics, Bristol, ROYAUME-UNI, 1991.

[24] G. Boothroyd, W.A. Knight, Fundamentals of machining and machine tools, Taylor and Francis, 2006.

[25] C. Arcona, T.A. Dow, An empirical tool force model for precision machining, Journal of Manufacturing Science and Engineering 120 (1998) 700–707.